



# Modulation of electronic spin state and construction of dual-atomic tandem reaction for enhanced pH-universal oxygen reduction

Lilian Wang<sup>a</sup>, Qi An<sup>a</sup>, Xuelin Sheng<sup>a</sup>, Zhiyuan Mei<sup>a</sup>, Qi Jing<sup>a</sup>, Xinyu Zhao<sup>a</sup>, Qijun Xu<sup>a</sup>, Lingyan Duan<sup>a</sup>, Xiaoxiao Zou<sup>a</sup>, Hong Guo<sup>a,b,\*</sup>

<sup>a</sup> International Joint Research Center for Advanced Energy Materials of Yunnan Province, Yunnan Key Laboratory of Carbon Neutrality and Green Low-carbon Technologies, School of Materials and Energy, Yunnan University, Kunming 650091, China

<sup>b</sup> Southwest United Graduate School, Kunming 650091, China

## ARTICLE INFO

### Keywords:

Spin-state regulation  
Orbital interaction  
Pair hardness  
Tandem reaction  
PH-universal ORR

## ABSTRACT

Combining both advances of electronic spin state modulation and tandem reaction mechanism, an atomic-level dual iron-copper catalyst is designed for enhanced oxygen reduction capability. Herein, the intense interaction between the iron-copper site and its coordination environment can not only controls the flow of external charge at the atomic level, but regulates the internal 3d electron configuration. These modulations can optimize the orbital interaction and pair hardness ( $\eta_{DA}$ ) between the acceptor and the donor, and achieves a fast tandem reaction kinetics, thereby surmounting the limitation of Scaling Relation. The as-prepared bimetal catalyst validates a high ORR activity and stability, which even exceed those of the benchmark Pt/C in pH-universal electrolytes. Meanwhile, Fe,Cu/N-C driven Zn-air batteries in alkaline and neutral electrolytes show prominent performance with peak power densities of 173.7 mW cm<sup>-2</sup> and 86.5 mW cm<sup>-2</sup>. This work provides a useful design principle for developing or optimizing other efficient ORR catalysts.

## 1. Introduction

The staggering increase in carbon dioxide has been generating a pressing requirement for clean energy technologies without delay [1]. Zn-air batteries are promising clean and sustainable energy conversion devices, and their tardy oxygen reduction reaction (ORR) on the air-cathode demands high-efficiency catalysts to boost the reaction kinetics [2,3]. However, the binding energies of closely related ORR intermediates over the single catalytic sites cannot be independently regulated due to the insurmountable Scaling Relation, which has been becoming a bottleneck to further improve its kinetics [4,5]. To overcome this conundrum, one important route is to simultaneously optimize the adsorption of each intermediate through spin regulation of the active site. This is inspired by the fact that the ORR between the initial triplet O<sub>2</sub> reactant and the final singlet H<sub>2</sub>O/OH<sup>-</sup> product with a different spin state is often slow or spin-forbidden [6–8]. Interestingly, when downsizing nanoparticles to single atoms, the atomically dispersed metal sites whose spin state, electronic density of state, band gap, and surface oxidation states of can be significantly modulated [9–12]. For instance, a

dual metal (M1,M2/N-C) catalyst demonstrates favorable ORR performance, which could be ascribed to the high activation of atomically dispersed M1-N sites by adjacent M2-N moieties through spin-state transition and electronic modulation [13–17]. Another available approach is to promote the adsorption of \*O<sub>2</sub>, and meanwhile, to accelerate the dissociation of \*OH through a dual-site tandem reaction mechanism, thus directly speeding up the reaction kinetics and surmounting Scaling Relation.

Though both strategies are resultful, most of current reports involve spin regulation alone, resulting in limited improvement of ORR performance. Particularly, rarely corresponding mechanism analysis has been conducted deeply. Therefore, designing a dual-site mechanism combining an ideal spin regulation and fast tandem reactions is an appropriate choice to achieve excellent ORR performance. In fact, too long intermetallic distance in single-site (M1-N-C) catalysts often restricts the interaction between adjacent metal atoms, resulting in that the metal sites are easily blocked by the Scaling Relation among different adsorption energies of ORR intermediates [18,19]. On the other hand, too short separation easily occasion two-electron reaction

\* Corresponding author at: International Joint Research Center for Advanced Energy Materials of Yunnan Province, Yunnan Key Laboratory of Carbon Neutrality and Green Low-carbon Technologies, School of Materials and Energy, Yunnan University, Kunming 650091, China.

E-mail address: [guohong@ynu.edu.cn](mailto:guohong@ynu.edu.cn) (H. Guo).

<https://doi.org/10.1016/j.apcatb.2023.123509>

Received 25 July 2023; Received in revised form 1 November 2023; Accepted 10 November 2023

Available online 14 November 2023

0926-3373/© 2023 Elsevier B.V. All rights reserved.

paths, such as for metal nanoparticles [18,20]. Therefore, precise design of M1,M2/N-C catalysts with an appropriate interatomic spacing between adjacent metallic active sites is a key solution to realize both the virtues of the two methods mentioned above and overcome the Scaling Relation limitation of M1-N-C catalysts. However, how to facilitate regulate the electron spin state and accompany a fast four-electron tandem reaction path, as well as the corresponding in-depth mechanism explanation, also remains extremely challenging.

Herein, a novel atomically dispersed Fe,Cu/N-C catalyst is designed as an example to illustrate our concept. This project combines both the advances of electronic spin state modulation and tandem reaction mechanism for enhanced ORR performance. The theoretical calculations and advanced analysis reveal that enhanced ORR performance stems from the spin state transition at the metal site and fast four-electron tandem reaction, which jointly promote  $^*O_2$  adsorption and  $^*OH$  desorption thermodynamically and kinetically. The in-depth mechanism studies based on both molecular orbital theory and pair hardness ( $\eta_{DA}$ ) further indicate that medium spin Fe cations provide the appropriate adsorption toward each intermediate, thus allowing excellent ORR performance under pH-universal conditions. It can be expected that the combination of both spin regulation and tandem reaction will exhibit an excellent oxygen electrocatalysis.

## 2. Experimental

This section is provided in the [Supplementary Material](#).

## 3. Results and discussion

### 3.1. Theoretical computation

Previous theoretical studies have reported that Cu holds the supreme ORR performance among nonprecious metal catalysts because, at the ‘volcano plot’, it is close to the Pt position [21]. In addition, the atomic structural similarity of Cu and Fe can minimize the destruction of Fe-N bonds caused by the introduction of an external Cu atom. Thus, Cu is a potential pairable candidate with Fe, with a strong bonding force with Fe and high freedom for both spin and charge modulation.

In this work, DFT calculations were first performed to penetrate the ORR active nature of Fe,Cu/N-C. The density of states (DOS) was examined to evidence the interaction between atomically dispersed Fe and Cu. As displayed in Fig. 1a and Fig. S1, the sharp peaks of both Fe (Fe/N-C) and Cu (Cu/N-C) sites are observed near the Fermi level, especially the sharper peaks of Fe, indicating that Fe sites bond to upcoming  $O_2$  more strongly than Cu sites [14]. Intriguingly, Fe,Cu/N-C catalysts under the collaboration of both Fe and Cu populate more spin-polarized electrons near the Fermi level. These spin-polarized itinerant electrons in the stray field caused by the spin-polarized Fe, Cu/N-C are more facilely to bond with two unpaired  $\pi^*$  electrons with the same spin-orientation of the triplet  $O_2$ , thereby strengthening the absorption of  $O_2$  in the initial ORR step [22]. This inference is also confirmed by calculating the active site coordinated by OH and  $O_2$ , respectively, which stems from the electrolysis of water and the adsorption of oxygen molecules during the electrocatalytic processes (Figs. S3-S9). The above theoretical calculations elucidate that Fe 3d electronic spin state in  $FeN_4$  can be easily modulated by adjacent metal sites. This spin-state regulation is expected to have an obvious effect on

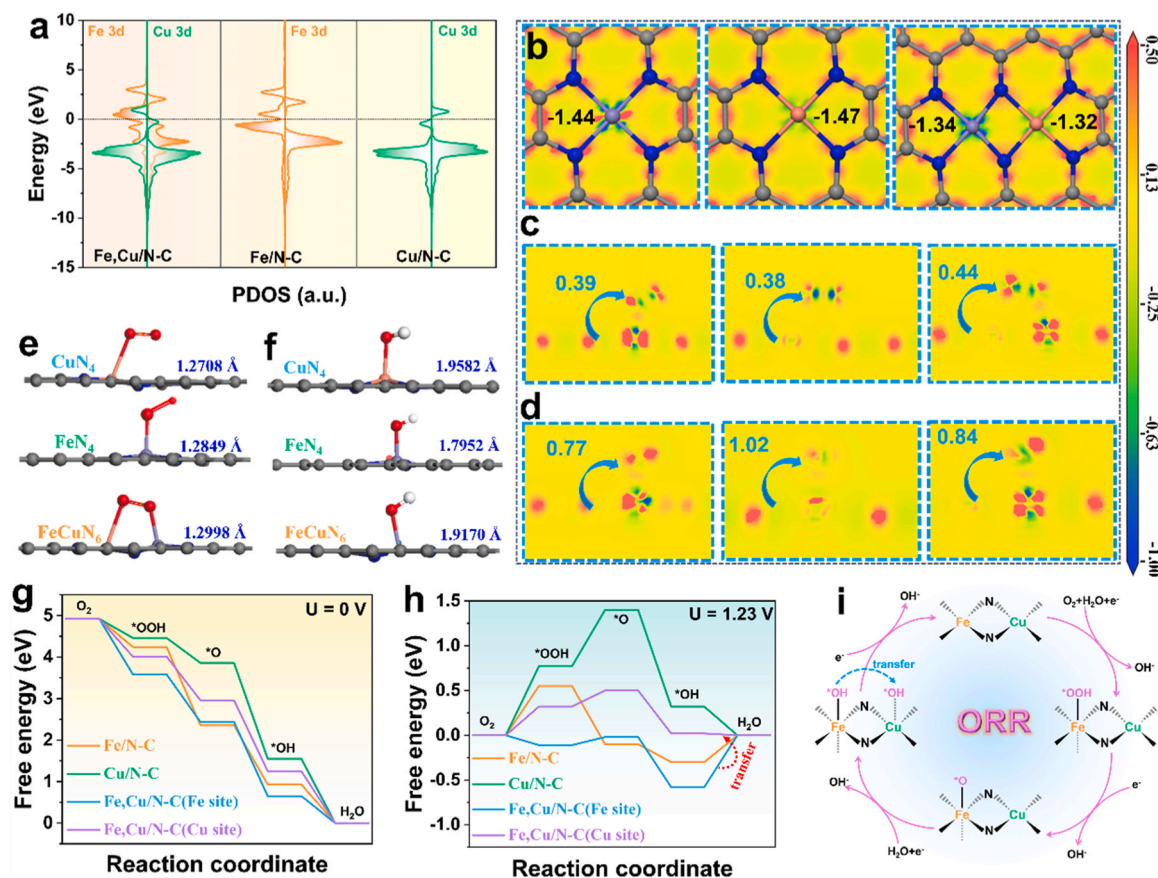


**Fig. 1.** a) DOS of as-prepared catalysts. b) Charge density difference and Bader charge of Fe/N-C, Cu/N-C and Fe,Cu/N-C. The Bader charges transfers from Fe/N-C, Cu/N-C and Fe,Cu/N-C to c)  $O_2$  and d) OH. The length of e) O-O bond and f) M-O bond with  $O_2$  and  $^*OH$  adsorbed on three models. ORR free energy diagrams at g) 0 V and h) 1.23 V. i) Scheme of tandem reaction mechanism on Fe,Cu/N-C.

ORR catalytic activity, being indeed demonstrated in the experimental test section.

To intuitively understand the origin of enhanced ORR activity in the Fe moiety introduced by the Cu atoms, the differential charge density map and Bader charge of catalysts were further calculated. The transferred charge number from the Fe center is 1.44 e in Fe/N-C, and decreased to 1.34 e after adding Cu. It can be observed from Fig. 1b and Fig. S2 that the formation of dual-metal pairs can significantly increase the charge density of the metal sites. Notably, albeit the charge density around non-metallic atoms far outperforms that around the central metal, metal atoms with partially empty 3d orbitals are more suitable for bonding with the orbitals of oxygen species during the ORR process relative to the energy level of both N 2p and C 2p, due to the principle of molecular orbital bonding [23–25]. Consequently, the central metal atoms are still considered to be the main catalytic active sites and have been investigated in detail in the magnetic measurements below. Moreover, the Bader charge group between the metal site and O<sub>2</sub> shows that Fe,Cu/N-C (0.44 e) transfers more electrons to O<sub>2</sub> than both Fe/N-C (0.39 e) and Cu/N-C (0.38 e) (Fig. 1c and Fig. S9), revealing that O<sub>2</sub> is more easily activated. This result is consistent with that implied by the length of O-O bond (Fig. 1e). Likewise, compared to Fe/N-C (0.77 e) and

Cu/N-C (1.02 e), Fe,Cu/N-C (0.84 e) transfers an appropriate number of electrons to OH (Fig. 1d and Fig. S6), indicating that neither too strong nor too weak adsorption is very beneficial for the final step during the oxygen reduction. The same results are obtained in the calculation of the M-OH bond length (Fig. 1f).

DFT calculations were also implemented to acquire ORR barriers catalyzed by Fe,Cu/N-C and other controls. Given that Fe,Cu/N-C possibly contains both Fe and Cu active centers, the ORR pathway on two sites was calculated. At a potential  $U = 0$  V, for Fe,Cu/N-C, all the stages from initial O<sub>2</sub> to final H<sub>2</sub>O are downgrade, revealing a facile reaction (Fig. 1g). Moreover, due to lower energy barriers on Fe sites than those on the Cu site in the first two steps, the conversion of O<sub>2</sub> molecular into \*OOH and \*O intermediates priorly occurs at Fe sites of Fe,Cu/N-C (Fig. 1h). Subsequently, since the energy barrier of the Cu site is much lower than that of the Fe site, \*OH species generated in the third step will be subsequently transferred from Fe sites to Cu sites following a tandem reaction mechanism. This significantly accelerates the dissociation of the metal-OH bond [26,27]. Hence, the existence of dual active centers in Fe,Cu/N-C can surmount the limitation of detrimental Scaling Relation in oxygen reduction. Fig. 1i exhibits the scheme of this tandem reaction mechanism on Fe,Cu/N-C.

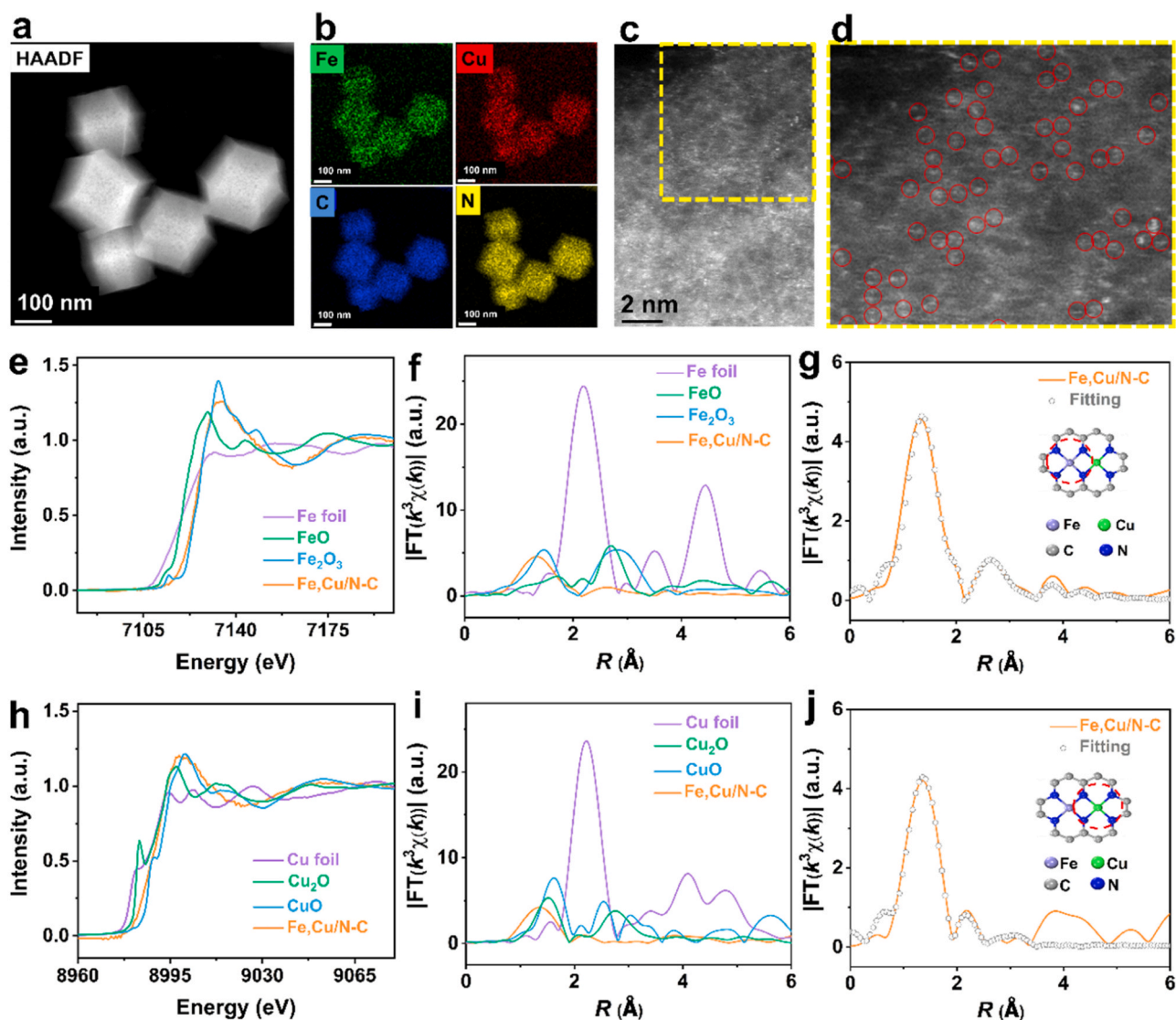


Fig. 2. a) HAADF-STEM image and b) EDS mapping of Fe,Cu/N-C. c) AC-HAADF-STEM and d) enlarged image of Fe,Cu/N-C. e) XANES of Fe K-edge, and f) FT EXAFS in R space for Fe,Cu/N-C and reference samples. g) Corresponding EXAFS fitting curves at the Fe K-edge of Fe,Cu/N-C. h) XANES of Cu K-edge, and i) FT EXAFS in R space for Fe,Cu/N-C and reference samples. j) Corresponding EXAFS fitting curves at the Cu K-edge of Fe,Cu/N-C.



### 3.2. Analysis of catalysts

To catch the evidence of high ORR catalytic capability of the prepared catalysts, we conducted a series of physical characterization experiments. The morphology of Fe,Cu/N-C shows a slightly bumpy polyhedral shape after pyrolysis (Fig. S10), and no metal clusters or nanoparticles are found by employing the high-angle annular dark-field scanning transmission electron microscope (HAADF-STEM) (Fig. 2a). Correspondingly, the energy-dispersive X-ray spectroscopy (EDS) demonstrates the uniform dispersion of Fe, Cu, C and N (Fig. 2b). Moreover, the evidence at atomic resolution of Fe and Cu distribution was acquired by using the aberration-corrected HAADF-STEM. As exhibited in Fig. 2c, the results consistent with EDS are obtained that small bright spots are evenly distributed in carbon support, assigned to heavy Cu, Fe than light C, N atoms [28]. Further enlarged as in Fig. 2d, many bright dual spot-pairs are observed as highlighted by red cycles. Moreover, the XRD patterns for each sample contain broad peaks at 24° and 44° (Fig. S11), arising from the (002) and (100) planes of graphite [29]. However, no diffraction peaks corresponding to metal species cannot absolutely eliminate the existence of other noncrystalline MN<sub>4</sub>-like metal species, due to the low sensitivity of XRD. As displayed in this contribution below, we wisely adopted more sensitive <sup>57</sup>Fe Mössbauer spectroscopy and X-ray absorption fine structure (XAFS) to identify atomically dispersed metals [30].

To probe the valence and coordination of Fe,Cu/N-C, X-ray absorption near-edge structure (XANES) and extended XAFS (EXAFS) measurements were conducted. Fig. 2e, h exhibit XANES results of the Fe and Cu K-edge in Fe,Cu/N-C and reference samples, respectively. The location of Fe,Cu/N-C absorption edge indicates that the valence state of Fe is between + 2 and + 3, and that of Cu is between + 1 and + 2 [31,32]. To obtain more structure information, the Fourier-transformed (FT) k<sup>2</sup>-weighted  $\chi(k)$  function of the EXAFS (FT EXAFS, without phase correction) was employed. As we can see from Fig. S12, FT EXAFS in k space for Fe,Cu/N-C at the Fe K edge and Cu K edge reveal the ascendancy of low Z back scatters, due to no oscillations in the high k region of  $k > 8 \text{ \AA}^{-1}$  [14,33]. In the FT EXAFS (R space) (Fig. 2f) of Fe,Cu/N-C, a major peak at 1.5 Å for Fe K edge is assigned to the Fe-N scattering paths, and the highest Fe-Fe peak near 2.18 Å in Fe foil is absent in Fe,Cu/N-C, further establishing atomically dispersed Fe species. At the same time, a small peak near 2.49 Å is observed, indicating the formation of the Fe-Cu pairs [34]. Similar to the analysis of Fe K edge, a main peak at 1.41 Å can also be seen for Cu K edge, corresponding to the Cu-N coordination scattering (Fig. 2i). The EXAFS fitting analysis can better reveal the structure of Fe,Cu/N-C sample (Fig. 2g, j and Table S1). The first shell coordination number of Fe-N is about 4, indicating the Fe site is coordinated with 4 N atoms. The Fe-Cu coordination is given by CN<sub>Fe-Cu</sub> = 0.8 ± 0.2 in the second shell, implying the generation of a weak Fe-Cu interaction. Also, the Cu-N coordination (CN = 4) and a weak coordination from Cu-Fe (CN = 0.4 ± 0.2) are obtained. These fitting results demonstrate the presence of FeCuN<sub>6</sub> structure in Fe, Cu/N-C, as shown in the theoretical model (inset in Fig. 2g, j). In combination with XAFS and the aforementioned microstructure analysis, the atomically dispersed Fe and Cu sites are well evidenced.

The chemical compositions of Fe,Cu/N-C were further investigated by X-ray photoelectron spectroscopy (XPS). Fig. S13a presents the peaks of Cu 2p assigned to Cu(I), Cu (II) and the satellite peak, respectively. The N 1s spectrum illustrates that there are five N species in Fe,Cu/N-C (Fig. S13b) [31]. Particularly, the existence of Fe/Cu-N (398.79 eV) is assigned to the atomically dispersed metal sites in Fe,Cu/N-C. The binding energy of metal-N in Fe,Cu/N-C surpasses that in Fe/N-C and is close to that in Cu/N-C, denoting that the addition of Cu (higher electronegative than Fe) can improve the electron density around the metal sites [35]. Moreover, as depicted in Table S2, the doping of Cu atoms enables the concentration of graphitic N (403.66 eV) to increase against Fe/N-C, thereby enhancing the stability of catalysts due to the formation of less defective and highly ordered graphitic carbon [36]. Compared

with N-C, the peaks of pyrrolic N in Fe/N-C, Cu/N-C, and Fe,Cu/N-C move toward higher binding energy, indicating that the lone pairs on pyrrolic N tends to contribute electrons to the metals [37]. The C 1s spectra are fitted into C=C, C-C, C-N, and C-O peaks (Fig. S13c). No obvious Fe signal was detected because Fe content was below the detection limit, which is consistent with previous reports (Fig. S13d) [14,34]. In the typical XPS wide scan spectrum of Fe,Cu/N-C, the approximate content of Cu and Fe may support the formation of Fe-Cu pairs (Table S3). As displayed in Table S4, the content of bimetals was determined to be 0.112 (Fe) and 0.111 (Cu) wt% by inductively coupled plasma optical emission spectrometry (ICP-OES). Raman spectroscopy is a sensitive technique for detecting the structure of carbon materials. The intensity ratio of D band (sp<sup>3</sup>) to G band (sp<sup>2</sup>), expressed as I<sub>D</sub>/I<sub>G</sub>, is often employed to estimate its defect, lattice disorder, and crystallinity [38]. In Fig. S14, the I<sub>D</sub>/I<sub>G</sub> ratios for Fe,Cu/N-C, and Fe/N-C and Cu/N-C are found to be 1.09, 1.02 and 1.13, respectively, signifying that a decrease in the average size of the sp<sup>2</sup> domains upon the introduction of Cu atoms.

Furthermore, electron paramagnetic resonance (EPR), <sup>57</sup>Fe Mössbauer spectroscopy and zero-field cooling (ZFC) temperature-dependent magnetic susceptibility (M-T) measurements were employed to analyze electronic spin-states of Fe and Cu active sites experimentally. EPR spectra present significant changes in peak shape and position among the resultant samples. Generally, the interaction between unpaired electrons and their environment and the change of angular momentum of unpaired electrons can affect the EPR peak shape and the value of g factor, respectively [39,40]. The highest g-factor value (g = 2.08) of bimetal catalyst reflects its highest content of unsaturated moieties with the unpaired electrons (Fig. S15) [41]. These results convincingly prove that the electronic spin-state of the FeN<sub>4</sub> site has indeed changed. ZFC temperature-dependent magnetic susceptibility test further demonstrate electronic spin-states of Fe and Cu sites in the resultant catalyst. Fig. 3a displays the number of unpaired 3d electrons for metal sites, determined by using the following equation [41]:

$$2.828 \sqrt{\chi_m T} = \mu_{\text{eff}} = \sqrt{n(n+2)}.$$

Typically, materials with unpaired electrons are called paramagnetic, and the opposite one is diamagnetic. As expected, it can be observed from Fig. 3a that the formation of Fe-Cu pairs significantly enhanced the paramagnetic state of the catalyst. The reason is that the d-orbitals of Cu can induce spin splitting in subtle Fe sites and excite electrons near the Fermi level of the active center. The unpaired 3d electron number (n) of the Fe/N-C catalyst is ~1, meaning Fe sites possess a low spin (LS) state mixed with Fe<sup>2+</sup> and Fe<sup>3+</sup>. However, the unpaired 3d electron number (n) of Fe,Cu/N-C is near 3, suggesting that Fe site in the FeN<sub>4</sub> moiety transforms from a low to a medium spin (MS) state mixed also with Fe<sup>2+</sup> and Fe<sup>3+</sup> after coupling FeN<sub>4</sub> with CuN<sub>4</sub>. This mixed valence is also very consistent with the XANES result. Apparently, the introduction of Cu with a sole spin state into the atomic site stimulates Fe sites to form a higher spin state, resulting in more unpaired electrons (Pauli paramagnetic free electrons). Specifically, a pair of electrons in the d<sub>xy</sub>(Fe<sup>2+</sup>)/d<sub>yz</sub>(Fe<sup>3+</sup>) orbital are decoupled so that one electron is stimulated to d<sub>z</sub><sup>2</sup> orbital for achieving Fe<sup>2+/3+</sup> with an MS configuration. We further analyze Fe 3d orbitals configurations to explain this phenomenon. Both orientation and transformation of five orbitals of Fe 3d are exhibited in Fig. 3c. These are energetically reasonable configurations in line with Hund rule and Pauli exclusion principle. Notably, π\*-orbitals of O<sub>2</sub> molecules could be easily penetrated by the single d<sub>z</sub><sup>2</sup> electrons of medium-spin Fe sites in Fe,Cu/N-C, resulting in a favorable ORR activity [14,22]. This also will be validated in the subsequent catalytic tests.

<sup>57</sup>Fe Mössbauer spectroscopy is a forceful technique for quantitatively discriminating iron species, particularly for those iron species with analogous coordinated environments but distinct electron configurations. As exhibited in Fig. 3b and Table S3, D1 doublet is found to be dominant in Fe,Cu/N-C. This D1 doublet is typically associated with the middle-spin (D1 doublet, Fe<sup>2+</sup> or Fe<sup>3+</sup>) in previous reports about the

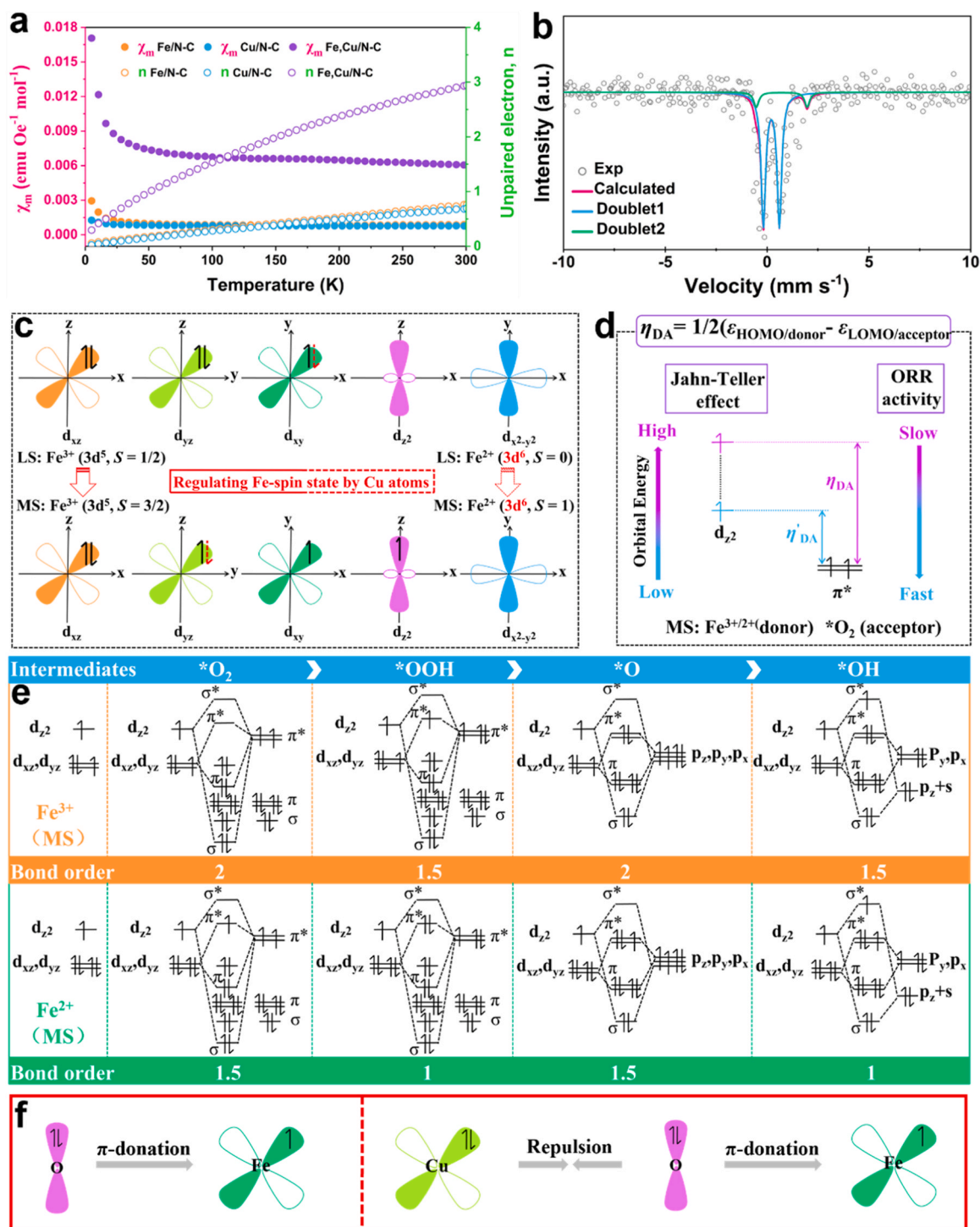


**Fig. 3.** a) M-T curves and the determined number of unpaired 3d electrons of all samples. b) <sup>57</sup>Fe Mössbauer spectrum of Fe,Cu/N-C. c) The transformation and orientation of the five d orbitals. d) The pair hardness ( $\eta_{DA}$ ) between donor \*Fe over Fe,Cu/N-C and acceptor \*O<sub>2</sub>. e) The orbital interactions between iron cations over Fe,Cu/N-C and oxygen-containing intermediates. f) Scheme of d<sub>xy</sub> electron interaction of Fe/N-C and Fe,Cu/N-C, respectively.

carbon-based N-doped Fe catalysts, confirming that Fe sites in Fe,Cu/N-C exist predominantly in medium-spin states [14,41]. The absence of singlet and sextet denotes no zero-valent iron crystalline phases. Meanwhile, a small fraction of other high-spin (Fe<sup>2+</sup> with S=2, D2 doublet) species is found in Fe,Cu/N-C. These results manifest that the spin state of the Fe site in Fe,Cu/N-C is transformed by the short-range electron interaction between Fe and Cu atomic sites, in agreement with ZFC analysis.

Importantly, on the basis of molecular-orbital theory, the role of Fe-

spin state regulation during ORR can be further understood through detailed analysis of the local spin configurations. The possible orbital interactions between iron cations over the whole surface of Fe,Cu/N-C and oxygen-containing intermediates are presented in Fig. 3e and Fig. S16. During the ORR process, the degree of orbital hybridization between d-orbitals of Fe sites and  $\pi_{2p}^*/2p$  orbitals of oxygen species will determine its bonding strength. Therefore, various local spin configurations could be rendered through filling different number of unpaired electrons into the d frontier orbitals, altering the hybridization energy

with intermediates. Thermodynamically, in order to promote the capture of reactants and the continuous release of products, a favorable/ideal ORR electrocatalyst should ensure strong absorption of  $^*O_2$  and weak absorption of  $^*OH$ . Quantitatively, the bond order of  $^*OH$  on the metal site is smaller than that of  $^*O_2$  on the metal cation [42]. We have analyzed the bond order of metal cations bonding to each intermediate in order to quantify the adsorption intensity. The bond order, as a descriptor of adsorption strength, can be determined by the equation below:

$$\text{Bond order} = \frac{n - n^*}{2}$$

in which  $n$  or  $n^*$  represent the number of bonding or antibonding electrons, respectively. The larger value of bond order, the stronger orbital interaction between intermediates and metal cations. As shown in Fig. 3e and Fig. S16, on account of the spin-orbital interactions, the bond orders of  $^*O_2$  bound to  $Fe^{2+/3+}$  (LS),  $Fe^{2+}$  (MS),  $Fe^{3+}$  (MS) and  $Cu^{2+/1+}$  are 1, 1.5, 2 and 1, respectively. Compared with both LS cations and Cu cations, the higher bond order values indicate a stronger orbital interaction between MS cations and the reaction intermediates, which is more favorable for starting ORR cycles. Moreover, on  $Fe^{2+/3+}$  (LS) and  $Fe^{2+}$  (MS) sites,  $^*OH$  shows 1.5 and 1 of bond order, respectively; while a lower bond order on  $Cu^{2+/1+}$  site is 0.5. Combining with the tandem reaction mechanism demonstrated in the theoretical calculation section (Fig. 1h, i), ORR process emerges the thermodynamic advantage of product release. Apparently,  $Fe^{2+/3+}$  with moderate spin polarization and Cu cations with synergistic effect present the required bond order values with intermediates, which can easily bond to oxygen species and rapidly dissociate the metal-OH bond to guarantee the recycle of  $O^*$  and  $OH^*$ , achieving a faster ORR kinetic process [36]. For the  $d_{xy}$  orbitals, Cu cations are occupied fully except for Fe (MS) cations with one unpaired electron. As shown in Fig. 3f, the filled  $\pi$ -symmetry  $d_{xy}$  of  $Cu^{2+}$  would give rise to the electronic repulsion between O and Cu orbital, which can be able to strengthen the  $\pi$ -donation between Fe and O. Thus, the doped Cu cations can vary the electron structure and accelerate the electron transfer.

Ultimately, for this two-partner reaction, the pair hardness ( $\eta_{DA}$ ) is defined as one-half of the energy gap between LUMO of acceptor and HOMO of donor, being another frequently-used reactivity index [43]. HOMO in the donor could overlap with LUMO in the acceptor, allowing a reaction to occur. Thus, the strength of the interaction between donor and acceptor depends on the energy gap between involved orbitals. The lower the  $\eta_{DA}$ , the higher the reactivity. In this work, the pair hardness ( $\eta_{DA}$ ) can be expressed as the energy gap between the  $d_z^2$  orbital of the metal ions (donor) and the  $2p/\pi_{2p}^*$  orbital of molecular oxygen (acceptor) (Fig. 3d). Additionally, according to the redox mechanism, ORR onset potential is strongly linked to the redox potential of metal ions, in turn naturally representing the energy level of the  $d_z^2$ -orbital [44]. As shown in Fig. 3d, since the  $d_z^2$ -orbitals of both Fe (MS) and Cu cations are unevenly occupied with the strong Jahn-Teller effect, this will lead to a decrease in the energy level of  $d_z^2$ -orbital. Therefore, this downshift of  $d_z^2$ -orbital can (i) effectively reduce the pair hardness ( $\eta_{DA}$ ) to optimize the bond intensity between metal sites and ORR oxygen-containing intermediates, and (ii) anodically alter metal ion's redox potential, thereby maximizing ORR onset potentials. In summary, all the above mechanism analyses clearly target the enhancement of ORR performance by overcoming the limitation of the detrimental Scaling Relation in oxygen reduction.

### 3.3. ORR catalytic capability

To evidence the highest ORR catalytic capability of Fe,Cu/N-C containing  $FeN_4$  (MS) moiety, using the rotating disk electrode with immobilized electrocatalysts evaluate the electrochemical performance of all catalysts. All potentials are provided versus reversible hydrogen

electrode (vs. RHE). As suggested by the results of linear sweep voltammetry (LSV) in Fig. 4a, c, Fe,Cu/N-C exhibits the highest oxygen catalytic activity in 0.1 M KOH solution albeit the metal loading is very low, featuring an exceptional half-wave potential ( $E_{1/2}$ ) of 0.86 V. This  $E_{1/2}$  is superior to Fe/N-C (0.79 V), Cu/N-C (0.77 V), those non-precious metal ORR catalysts reported previously (Tables S7, S10), and comparable to the Pt/C benchmark ( $E_{1/2} = 0.84$  V). CV tests with different sweep rates present the capacity of double layer ( $C_{dl}$ ) of  $36.8 \text{ mF cm}^{-2}$  of Fe,Cu/N-C is 5 times that of Pt/C ( $7.2 \text{ mF cm}^{-2}$ ), and also superior to Fe/N-C ( $33.9 \text{ mF cm}^{-2}$ ) and Cu/N-C ( $28.7 \text{ mF cm}^{-2}$ ) (Fig. S17). Strikingly, the mass activity (MA, proportional to kinetic current density ( $J_k$ )) of Fe, Cu/N-C ( $34 \text{ A g}^{-1}$ ) is 8, 18 and 2 times as high as that of Fe/N-C ( $4.29 \text{ A g}^{-1}$ ), Cu/N-C ( $1.82 \text{ A g}^{-1}$ ) and Pt/C ( $19.6 \text{ A g}^{-1}$ ), respectively (Fig. S18b). Notably, MA is a comprehensive indicator demonstrating the total apparent catalytic capability of catalysts per unit mass ( $MA = SA \times ECSA$ , an explicit correlation between MA, SA, and ECSA), in which ECSA (electrochemically active surface area) signifies the exposed active area of catalysts, and SA (specific activity) denotes the intrinsic catalytic capability of catalysts per unit exposed area.

The oxygen reduction kinetics was also investigated via the Tafel plot and Koutecky-Levich (K-L) method to reveal electronic transfer process on catalysts from the catalytic site to  $O_2$  [45,46]. As calculated in the light of the K-L equation, the electron transfer number ( $n$ ) of Fe,Cu/N-C is 3.91. Its K-L plot exhibits a good linearity correlation in the region of limit current ( $J_L$ ), confirming the first-order reaction kinetics for ORR (Figs. S19, S20). Moreover, with the increasing rotating speed,  $E_{onset}$  keeps a constant, and  $J_L$  of Fe,Cu/N-C gradually increases, resulting from the decreased concentration polarization at high rotating speed. Compared with those of other single metal and Pt/C reference catalysts, Fe,Cu/N-C displays a smallest Tafel slope of  $65 \text{ mV dec}^{-1}$ , confirming its favorable ORR kinetics (Fig. S18a).

Some reported single-site metal catalysts, because of their weak activation of  $O_2$ , exhibit high selectivity for  $H_2O_2$ . So, the  $H_2O_2$  yield and  $n$  were further probed by a rotating ring-disk electrode (RRDE). And RRDE results present a nearly absolute 4-electron pathway with  $H_2O_2$  yield below 2.5 % over all potentials with  $n \approx 4$  (Fig. 4b), verifying the key role of Fe-Cu pairs in the construction of 4-electron electrocatalytic processes. However, there is a difference in the result of  $n$  between the K-L method and RRDE. Because the ORR process is neither a one-way nor a single-step reaction, it does not follow the assumptions of the K-L method [47].

The stability of Fe,Cu/N-C is markedly improved after forming dual-metal sites, as demonstrated by just 1 mV loss of  $E_{1/2}$  after 5000 CV cycling in 0.1 M KOH, well beyond that of Fe/N-C (7 mV loss), Cu/N-C (6 mV loss) and Pt/C (18 mV loss) (Fig. S21). To further evaluate durability, Fe,Cu/N-C was continuously subjected to the chronoamperometry testing for 40,000 s, and the result displays a retention of 94.8 % of the initial current (Fig. 4j and Fig. S22). Furthermore, the XRD patterns (Fig. S23), TEM images (Fig. S24) and XPS spectra (Figs. S25-S28) of Fe,Cu/N-C and other controls exhibit no evident changes in microstructure and morphology after 40,000 s. The favorable durability of Fe,Cu/N-C in an alkaline condition is pivotally resulting from the structure of the robust  $Fe-N_4$  and  $Cu-N_4$  coordinated by pyrrolic N on the carbon support, preventing the aggregation and dissolution of Fe and Cu species [48,49]. Additionally, Fe,Cu/N-C displays a robust tolerance to  $CH_3OH$  with respect to Pt/C (Fig. S29).

Meanwhile, ORR activity mediated with Fe,Cu/N-C in neutral (0.1 M PBS) and acidic (0.5 M  $H_2SO_4$ ) media was also examined. Fe,Cu/N-C features  $E_{1/2}$  of 0.73 V in 0.1 M PBS (superior to 0.63 V of Pt/C) and 0.74 V in 0.5 M  $H_2SO_4$  (comparable to 0.77 V of Pt/C), which well exceeds those of Fe/N-C (0.50 V and 0.44 V, respectively) and Cu/N-C (0.45 V and 0.30 V, respectively) (Fig. 4d, f, g and i). Moreover, the lowest Tafel slopes of  $95 \text{ mV dec}^{-1}$  in 0.5 M  $H_2SO_4$  and  $121 \text{ mV dec}^{-1}$  in 0.1 M PBS for Fe,Cu/N-C validate its fastest ORR kinetics, relative to those of Pt/C (101 and  $155 \text{ mV dec}^{-1}$ ), Fe/N-C (295 and  $192 \text{ mV dec}^{-1}$ ), and Cu/N-C (320 and  $182 \text{ mV dec}^{-1}$ ) (Figs. S30a, S37a). Besides, Fe,Cu/



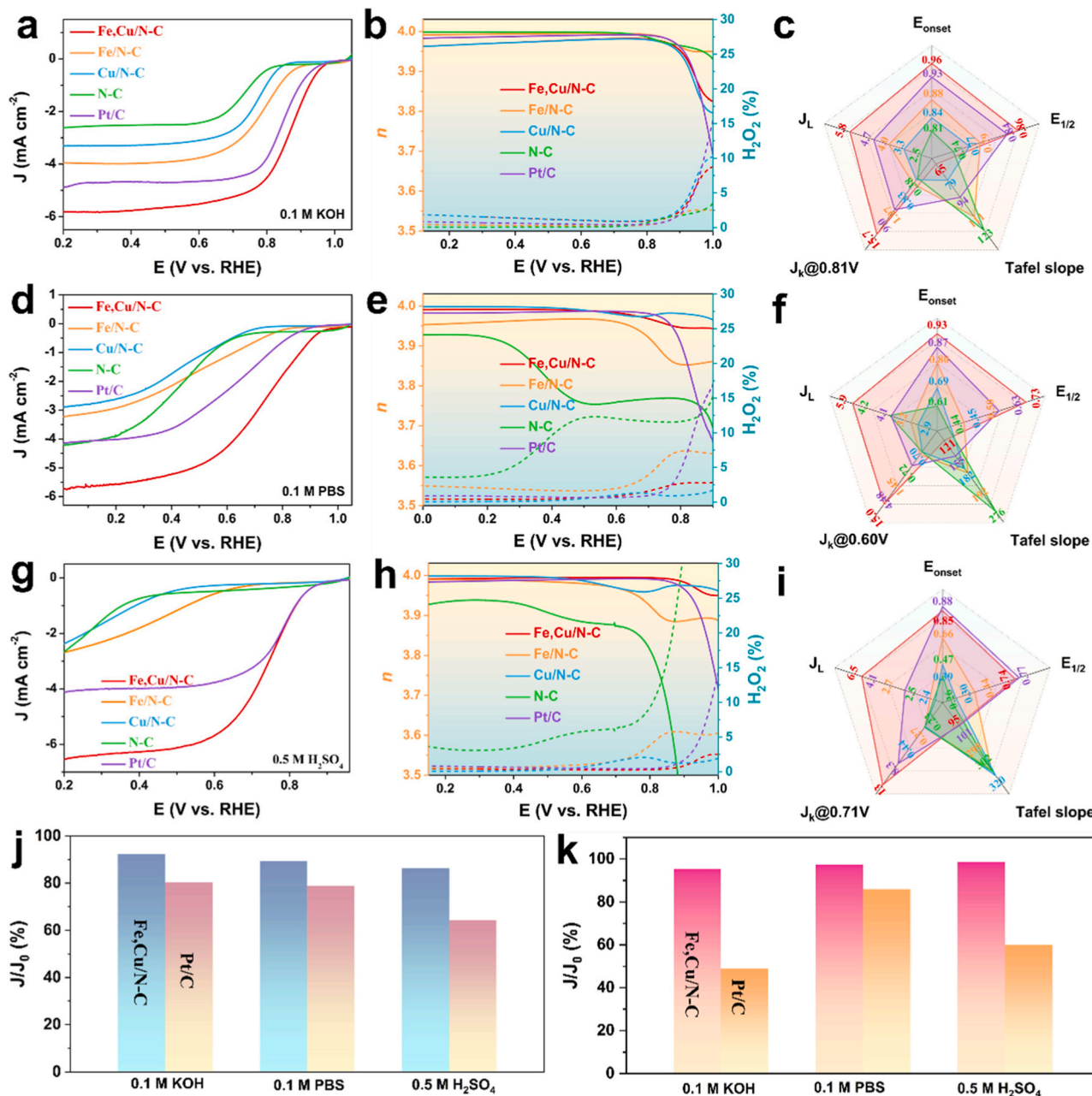


**Fig. 4.** ORR catalytic performance of Fe,Cu/N-C in pH-universal electrolytes. LSV polarization curves of Fe,Cu/N-C and other comparison samples in a) 0.1 M KOH, d) 0.1 M PBS, and g) 0.5 M  $\text{H}_2\text{SO}_4$ . The numbers of electron transfer ( $n$ ) and the yields of  $\text{H}_2\text{O}_2$  in b) 0.1 M KOH, e) 0.1 M PBS, h) 0.5 M  $\text{H}_2\text{SO}_4$ . Comparison of key parameters corresponding to LSV for all samples and Pt/C in c) 0.1 M KOH, f) 0.1 M PBS, i) 0.5 M  $\text{H}_2\text{SO}_4$  (the colors of parameters for the samples correspond to those of LSV curves). The chronoamperometric stability tests of Fe,Cu/N-C and Pt/C in pH-universal electrolytes j) for 40,000 s and k) after adding methanol.

N-C exhibits the highest kinetic current density ( $J_k$ ) of  $15 \text{ mA cm}^{-2}$  in 0.1 M PBS, which is 10, 20 and 3.3 times as high as those of single metal, and Pt/C, respectively (Fig. 4f). Likewise,  $J_k$  of  $13 \text{ mA cm}^{-2}$  of Fe,Cu/N-C in 0.5 M  $\text{H}_2\text{SO}_4$  also outperforms Pt/C and other controls (Fig. 4i). In addition, the testing results of RRDE in 0.1 M PBS and 0.5 M  $\text{H}_2\text{SO}_4$  signify that Fe,Cu/N-C possesses higher electron transfer numbers with lower yields for  $\text{H}_2\text{O}_2$  than the benchmark Pt/C and other controls (Fig. 4e, h). The average  $n$  of Fe,Cu/N-C is estimated to be 3.99, and the  $\text{H}_2\text{O}_2$  yields approach 2.5 % in neutral media, and in acid solution, these values are 3.95 % and 2.3 %, respectively. Accordingly, Fe,Cu/N-C follows a 4e process in both neutral and acidic conditions. Also, this result is confirmed by the K-L method (Figs. S32, S33, S39 and S40). The durability measurements exhibit that the retention rate for the current density of Fe,Cu/N-C is over 86.2 % in both neutral and acidic media

after chronoamperometry testing for 40,000 s (Figs. 4j and S42), and shows a negligible loss in  $E_{1/2}$  after cycling for 5000 cycles in the above two solutions (Figs. S34, S41). After adding  $\text{CH}_3\text{OH}$  to the electrolytes, the current density slightly decreased for Fe,Cu/N-C and other controls, and sharply decreased for Pt/C, evidencing the robust methanol tolerance of prepared catalysts (Figs. S36, S43). Consequently, Fe,Cu/N-C possess a great potential for applications in pH-universal conditions (Tables S8-S10).

In terms of both satisfactory ORR performance and stability, further, Fe,Cu/N-C was adopted to assemble Zinc-air batteries (ZABs) to validate its potential in the energy conversion device (see Supplementary Material for more details). Also, ZABs were constructed with Pt/C in the same procedure as a comparison. As expected, Fe,Cu/N-C enables the alkaline ZABs with both a good peak power density of  $173.7 \text{ mW cm}^{-2}$

and an open circuit voltage (OCV) of 1.31 V, outperforming those of Pt/C-driven battery ( $140.8 \text{ mW cm}^{-2}$  and 1.30 V) (Fig. 5a). The specific capacity is additionally evaluated to be  $817.7 \text{ mAh g}_{\text{Zn}}^{-1}$  via galvanostatically discharging according to the consumed zinc foil, which surpasses the Pt/C-based one ( $809.2 \text{ mAh g}_{\text{Zn}}^{-1}$ ) and some reported catalysts (Fig. 5b and Table S11). Subsequently, rate performance was investigated via galvanostatic discharge test at different current densities (Fig. 5c). The Fe,Cu/N-C-driven ZAB displays superb rate performance with higher discharge voltages than the Pt/C-driven one at all the current densities. Besides, the ZAB with Fe,Cu/N-C presents small voltage drops, and what's more, the discharge voltage can be quickly recovered when the current density returned to the same as before, manifesting its satisfactory reversibility. To broaden applications of Fe,Cu/N-C, rechargeable ZABs with Fe,Cu/N-C + RuO<sub>2</sub> (1:1) as the cathode catalyst were assembled, which displays the feasibility of long-term cycling to afford a life span over 1000 cycles while holding a voltage gap less than 0.74 V (Fig. 5d). As a contrast, the ZABs with Pt/C + RuO<sub>2</sub> (1:1) were also prepared under the same conditions and exhibit unsatisfactory working stability with a limited 400-cycle life span. Also, we can additionally discover that Fe,Cu/N-C + RuO<sub>2</sub>-driven ZAB possesses a lower charging-discharging voltage gap ( $\sim 0.73 \text{ V}$ ) than Pt/C + RuO<sub>2</sub>-based one, and an ultrahigh charge-discharge cycle life span over 171 h. Notably, the aforementioned impressive merits can be attributed to Fe-Cu pairs with the medium-spin state and the robust Fe-N<sub>4</sub> and Cu-N<sub>4</sub>

coordinated by pyrrolic N.

Given that both the safety and satisfactory ORR performance of neutral electrolytes, herein, Fe,Cu/N-C is also applied in homemade ZABs with the same structure. Interestingly, the performance of neutral ZAB with Fe,Cu/N-C well outperforms those of Pt/C-based one. Specifically, Fe,Cu/N-C-based ZAB can achieve a larger peak power density of  $86.5 \text{ mW cm}^{-2}$  than the Pt/C-based one ( $47.3 \text{ mW cm}^{-2}$ ), an OCV of 1.21 V well superior to Pt/C-based one (1.14 V) (Fig. 5a), higher voltage plateaus than Pt/C-based one at all different current densities (Fig. 5c). Also, Fe,Cu/N-C + RuO<sub>2</sub>-driven ZAB exhibits a higher/lower discharging/charging voltage than a Pt/C + RuO<sub>2</sub>-driven battery during the discharging-charging cycle for 171 h (Fig. 5e). Encouraged by the rising requirement for flexible wearable electronic devices, we further explored the flexible quasi-solid-state ZABs composed of Zn foil (anode), the catalysts loaded on carbon cloth (cathode) and solid polyacrylic acid electrolyte (Fig. 5f). The assembled flexible ZABs hold good mechanical flexibility, which still presents steady charge/discharge profiles upon several characteristic deformations (such as bending, twisting, folding, and cutting) (Fig. 5g). Obviously, Fe,Cu/N-C has great potential for applications in the field of flexible wearable electronics.

#### 4. Conclusion

In summary, atomically dispersed dual-metal Fe,Cu/N-C catalysts

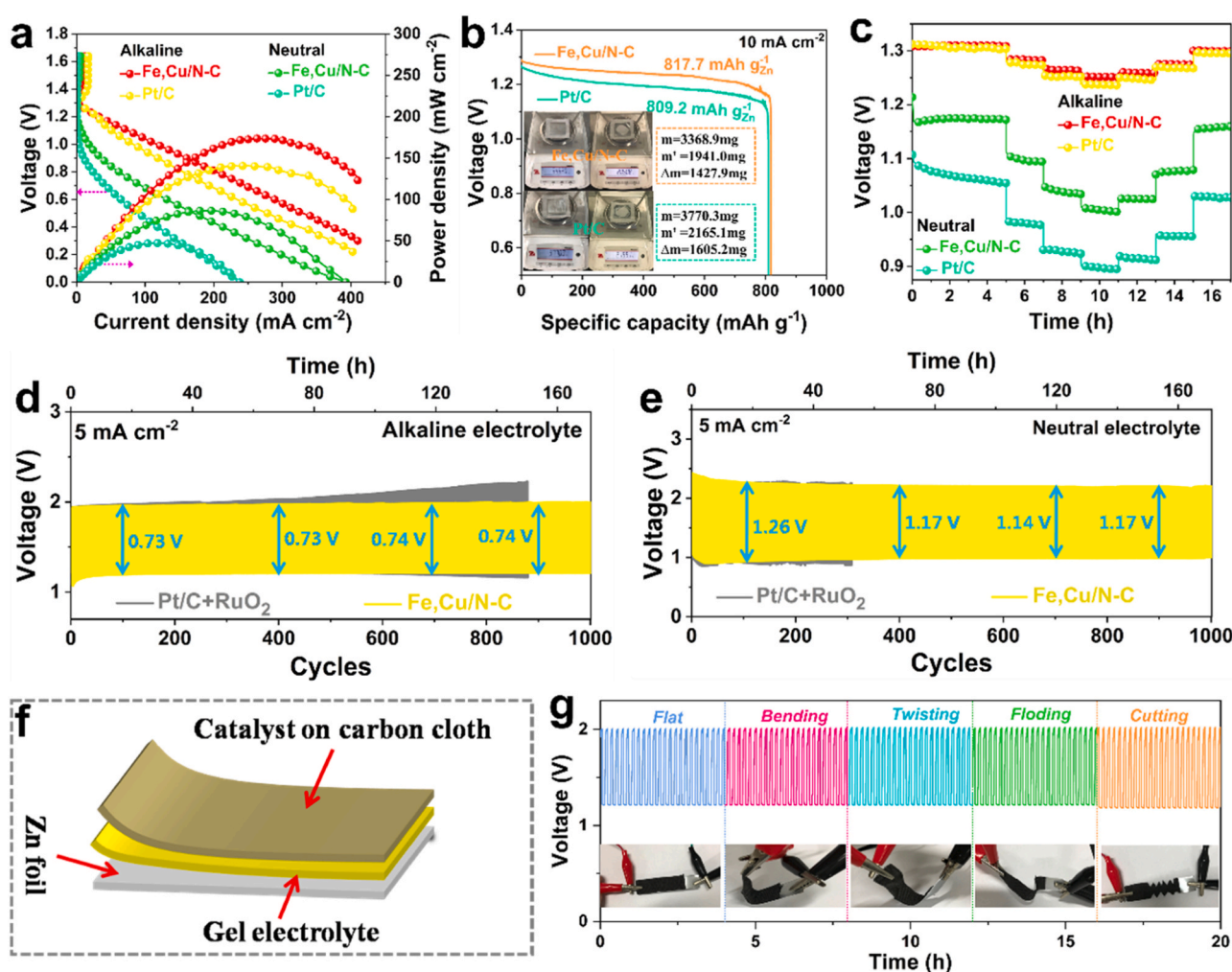


**Fig. 5.** a) Polarization and power density of alkaline and neutral ZABs driven by Fe,Cu/N-C and the benchmark Pt/C. b) Specific capacities of Fe,Cu/N-C, and Pt/C, normalized by the consumed Zn mass (inset). c) Galvanostatic discharge of both alkaline and neutral ZABs with Fe,Cu/N-C and Pt/C as electrocatalysts with different current densities. d) Contrast of galvanostatic discharge-charge cycling between two alkaline ZABs. e) Comparison of galvanostatic discharge-charge cycling between two neutral ZABs. f) Schematic illustration of a homemade flexible quasi-solid-state ZAB. g) Cycling plots of flexible ZAB upon different deformations.



involving both spin regulation and fast tandem reaction kinetics present superior ORR performance over a wide pH range relative to single Fe or Cu metal controls, exceeding those of the commercial Pt/C. Moreover, Fe/Cu/N-C catalysts exhibit a huge potential as the air cathodes for alkaline and neutral ZABs. Theoretical calculations have been evidenced that such splendid ORR performance originates from both localization/transition of charges/electronic spin state and tandem transfer of oxygen species on the dual-metal active centers. These changes do optimize the energy barrier and bond order of the ORR process. This contribution not only opens up fascinating routes to surmount the scaling relation limits in multiple-step reactions, but also provides a series of ideas for the development of renewable electronic devices.

### CRediT authorship contribution statement

**Lilian Wang:** Investigation, Writing – original draft, Writing – review & editing, Data curation, Formal analysis. **Qi An:** Data curation, Software. **Xuelin Sheng:** Formal analysis, Validation. **Zhiyuan Mei:** Data curation, Formal analysis. **Qi Jing:** Formal analysis, Software. **Xinyu Zhao:** Formal analysis, Software. **Qijun Xu:** Formal analysis, Software. **Lingyan Duan:** Formal analysis, Software. **Xiaoxiao Zou:** Investigation, Formal analysis. **Hong Guo:** Writing – review & editing, Funding acquisition, Supervision, Resources.

### Declaration of Competing Interest

The authors declare that they have no known competing financial interests or personal relationships that could have appeared to influence the work reported in this paper.

### Data availability

Data will be made available on request.

### Acknowledgements

The authors acknowledge the financial support provided by Major Science and Technology Projects of Yunnan Province (202302AB080019-3), the National Natural Science Foundation of China (52064049), National Natural Science Foundation of Yunnan Province (202301AS070040), Key Laboratory of Solid-State Ions for Green Energy of Yunnan University, the Electron Microscope Center of Yunnan University and the authors would like to thank Shiyanjia Lab (www.shiyanjia.com) for the SEM test.

### Appendix A. Supporting information

The chemicals, synthesis of catalysts, characterizations, electrochemical measurements, aqueous and flexible quasi-solid-state ZABs measurements and DFT calculations are shown in Supplementary Material. Supplementary data associated with this article can be found in the online version at [doi:10.1016/j.apcatb.2023.123509](https://doi.org/10.1016/j.apcatb.2023.123509).

### References

- [1] X. Li, Z. Xiang, Identifying the impact of the covalent-bonded carbon matrix to FeN<sub>4</sub> sites for acidic oxygen reduction, *Nat. Commun.* 13 (2022), <https://doi.org/10.1038/s41467-021-27735-1>.
- [2] C. Zhu, H. Li, S. Fu, D. Du, Y. Lin, Highly efficient nonprecious metal catalysts towards oxygen reduction reaction based on three-dimensional porous carbon nanostructures, *Chem. Soc. Rev.* 45 (2016) 517–531, <https://doi.org/10.1039/C5CS00670H>.
- [3] X. Xie, C. He, B. Li, Y. He, D.A. Cullen, E.C. Wegener, A.J. Kropf, U. Martinez, Y. Cheng, M.H. Engelhard, M.E. Bowden, M. Song, T. Lemmon, X.S. Li, Z. Nie, J. Liu, D.J. Myers, P. Zelenay, G. Wang, G. Wu, V. Ramani, Y. Shao, Performance enhancement and degradation mechanism identification of a single-atom Co–N–C catalyst for proton exchange membrane fuel cells, *Nat. Catal.* 3 (2020) 1044–1054, <https://doi.org/10.1038/s41929-020-00546-1>.
- [4] X. Zhu, C. Hu, R. Amal, L. Dai, X. Lu, Heteroatom-doped carbon catalysts for zinc-air batteries: progress, mechanism, and opportunities, *Energy Environ. Sci.* 13 (2020) 4536–4563, <https://doi.org/10.1039/d0ee02800b>.
- [5] M.T.M. Koper, Theory of multiple proton-electron transfer reactions and its implications for electrocatalysis, *Chem. Sci.* 4 (2013) 2710–2723, <https://doi.org/10.1039/c3sc50205h>.
- [6] S. Chretien, H. Metiu, O<sub>2</sub> evolution on a clean partially reduced rutile TiO<sub>2</sub>(110) surface and on the same surface precovered with Au1 and Au2: the importance of spin conservation, *J. Chem. Phys.* 129 (2008) 74705, <https://doi.org/10.1063/1.2956506>.
- [7] J. Gracia, Spin dependent interactions catalyse the oxygen electrochemistry, *Phys. Chem. Chem. Phys.* 19 (2017) 20451–20456, <https://doi.org/10.1039/C7CP04289B>.
- [8] S. Ghosh, B.P. Bloom, Y. Lu, D. Lamont, D.H. Waldeck, Increasing the efficiency of water splitting through spin polarization using cobalt oxide thin film catalysts, *J. Phys. Chem. C* 124 (2020) 22610–22618, <https://doi.org/10.1021/acs.jpcc.0c07372>.
- [9] Y. Shi, Y. Zhou, Y. Lou, Z. Chen, H. Xiong, Y. Zhu, Homogeneity of supported single-atom active sites boosting the selective catalytic transformations, *Adv. Sci.* 9 (2022) 1–40, <https://doi.org/10.1002/adv.202201520>.
- [10] Z.-X. Wei, Y.-T. Zhu, J.-Y. Liu, Z.-C. Zhang, W.-P. Hu, H. Xu, Y.-Z. Feng, J.-M. Ma, Recent advance in single-atom catalysis, *Rare Met* 40 (2021) 767–789, <https://doi.org/10.1007/s12598-020-01592-1>.
- [11] S. Sarkar, A. Biswas, E.E. Siddharthan, R. Thapa, R.S. Dey, Strategic modulation of target-specific isolated Fe,Co single-atom active sites for oxygen electrocatalysis impacting high power Zn-air battery, *ACS Nano* 16 (2022) 7890–7903, <https://doi.org/10.1021/acsnano.2c00547>.
- [12] G. Kumar, R.S. Dey, Coordination engineering of dual Co, Ni active sites in N-doped carbon fostering reversible oxygen electrocatalysis, *Inorg. Chem.* 62 (2023) 13519–13529, <https://doi.org/10.1021/acs.inorgchem.3c01925>.
- [13] R. Gao, J. Xu, J. Wang, J. Lim, C. Peng, L. Pan, X. Zhang, H. Yang, J.J. Zou, Pd/Fe<sub>2</sub>O<sub>3</sub> with electronic coupling single-site Pd-Fe pair sites for low-temperature semihydrogenation of alkynes, *J. Am. Chem. Soc.* 144 (2022) 573–581, <https://doi.org/10.1021/jacs.1c11740>.
- [14] G. Yang, J. Zhu, P. Yuan, Y. Hu, G. Qu, B.A. Lu, X. Xue, H. Yin, W. Cheng, J. Cheng, W. Xu, J. Li, J. Hu, S. Mu, J.N. Zhang, Regulating Fe-spin state by atomically dispersed Mn-N in Fe-N-C catalysts with high oxygen reduction activity, *Nat. Commun.* 12 (2021) 4–13, <https://doi.org/10.1038/s41467-021-21919-5>.
- [15] Y.-F. Wu, J.-W. Ma, Y.-H. Huang, Enhancing oxygen reduction reaction of Pt–Co/C nanocatalysts via synergetic effect between Pt and Co prepared by one-pot synthesis, *Rare Met* 42 (2023) 146–154, <https://doi.org/10.1007/s12598-022-02119-6>.
- [16] W. Jiao, C. Chen, W. You, X. Zhao, J. Zhang, Y. Feng, P. Wang, R. Che, Hollow palladium-gold nanochains with periodic concave structures as superior ORR electrocatalysts and highly efficient SERS substrates, *Adv. Energy Mater.* 10 (2020) 1–13, <https://doi.org/10.1002/aenm.201904072>.
- [17] H.-Y. Gong, X. Liang, G.-L. Sun, D.-W. Li, X.-J. Zheng, H. Shi, K. Zeng, G.-C. Xu, Y. Li, R.-Z. Yang, C.-Z. Yuan, Insight into role of Ni/Fe existing forms in reversible oxygen catalysis based on Ni-Fe single-atom/nanoparticles and N-doped carbon, *Rare Met* 41 (2022) 4034–4040, <https://doi.org/10.1007/s12598-022-02078-y>.
- [18] Z. Jin, P. Li, Y. Meng, Z. Fang, D. Xiao, G. Yu, Understanding the inter-site distance effect in single-atom catalysts for oxygen electroreduction, *Nat. Catal.* 4 (2021) 615–622, <https://doi.org/10.1038/s41929-021-00650-w>.
- [19] J. Chen, H. Li, C. Fan, Q. Meng, Y. Tang, X. Qiu, G. Fu, T. Ma, Dual single-atomic Ni-N<sub>4</sub> and Fe-N<sub>4</sub> sites constructing Janus hollow graphene for selective oxygen electrocatalysis, *Adv. Mater.* 32 (2020), 2003134, <https://doi.org/10.1002/adma.202003134>.
- [20] Y.-J. Ko, K. Choi, B. Yang, W.H. Lee, J.-Y. Kim, J.-W. Choi, K.H. Chae, J.H. Lee, Y. J. Hwang, B.K. Min, H.-S. Oh, W.-S. Lee, A catalyst design for selective electrochemical reactions: direct production of hydrogen peroxide in advanced electrochemical oxidation, *J. Mater. Chem. A* 8 (2020) 9859–9870, <https://doi.org/10.1039/D0TA01869D>.
- [21] J.K. Nørskov, J. Rossmeisl, A. Logadottir, L. Lindqvist, J.R. Kitchin, T. Bligaard, H. Jónsson, Origin of the overpotential for oxygen reduction at a fuel-cell cathode, *J. Phys. Chem. B* 108 (2004) 17886–17892, <https://doi.org/10.1021/jp047349j>.
- [22] Z. Li, Z. Zhuang, F. Lv, H. Zhu, L. Zhou, M. Luo, J. Zhu, Z. Lang, S. Feng, W. Chen, L. Mai, S. Guo, The marriage of the FeN<sub>4</sub> moiety and MXene boosts oxygen reduction catalysis: Fe 3d electron delocalization matters, *Adv. Mater.* 30 (2018) 1–8, <https://doi.org/10.1002/adma.201803220>.
- [23] Y. Zhou, S. Sun, J. Song, S. Xi, B. Chen, Y. Du, A.C. Fisher, F. Cheng, X. Wang, H. Zhang, Z.J. Xu, Enlarged Co–O covalency in octahedral sites leading to highly efficient spinel oxides for oxygen evolution reaction, *Adv. Mater.* 30 (2018), <https://doi.org/10.1002/adma.201802912>.
- [24] Y. Zhou, S. Sun, C. Wei, Y. Sun, P. Xi, Z. Feng, Z.J. Xu, Significance of engineering the octahedral units to promote the oxygen evolution reaction of spinel oxides, *Adv. Mater.* 31 (2019), <https://doi.org/10.1002/adma.201902509>.
- [25] S. Sun, Y. Sun, Y. Zhou, S. Xi, X. Ren, B. Huang, H. Liao, L.P. Wang, Y. Du, Z.J. Xu, Shifting oxygen charge towards octahedral metal: a way to promote water oxidation on cobalt spinel oxides, *Angew. Chem. Int. Ed.* 58 (2019) 6042–6047, <https://doi.org/10.1002/anie.201902114>.
- [26] A.L. Bouwkamp-Wijnoltz, W. Visscher, J.A.R. Van Veen, The selectivity of oxygen reduction by pyrolysed iron porphyrin supported on carbon, *Electrochim. Acta* 43 (1998) 3141–3152, [https://doi.org/10.1016/S0013-4686\(98\)00076-0](https://doi.org/10.1016/S0013-4686(98)00076-0).
- [27] J. Guan, Z. Duan, F. Zhang, S.D. Kelly, R. Si, M. Dupuis, Q. Huang, J.Q. Chen, C. Tang, C. Li, Water oxidation on a mononuclear manganese heterogeneous

- catalyst, *Nat. Catal.* 1 (2018) 870–877, <https://doi.org/10.1038/s41929-018-0158-6>.
- [28] G. Moon, M. Yu, C.K. Chan, H. Tüysüz, Highly active cobalt-based electrocatalysts with facile incorporation of dopants for the oxygen evolution reaction, *Angew. Chem. Int. Ed.* 58 (2019) 3491–3495, <https://doi.org/10.1002/anie.201813052>.
- [29] T. Gong, R. Qi, X. Liu, H. Li, Y. Zhang, N. F-codoped microporous carbon nanofibers as efficient metal-free electrocatalysts for ORR, *Nano Micro Lett.* 11 (1) (2019) 11, <https://doi.org/10.1007/s40820-019-0240-x>.
- [30] T.N. Huan, N. Ranjbar, G. Rousse, M. Sougrati, A. Zitolo, V. Mougél, F. Jaouen, M. Pontecave, Electrochemical reduction of CO<sub>2</sub> catalyzed by Fe-N-C materials: a structure-selectivity study, *ACS Catal.* 7 (2017) 1520–1525, <https://doi.org/10.1021/acscatal.6b03353>.
- [31] Z. Li, Y. Chen, S. Ji, Y. Tang, W. Chen, A. Li, J. Zhao, Y. Xiong, Y. Wu, Y. Gong, T. Yao, W. Liu, L. Zheng, J. Dong, Y. Wang, Z. Zhuang, W. Xing, C.-T. He, C. Peng, W.-C. Cheong, Q. Li, M. Zhang, Z. Chen, N. Fu, X. Gao, W. Zhu, J. Wan, J. Zhang, L. Gu, S. Wei, P. Hu, J. Luo, J. Li, C. Chen, Q. Peng, X. Duan, Y. Huang, X.-M. Chen, D. Wang, Y. Li, Iridium single-atom catalyst on nitrogen-doped carbon for formic acid oxidation synthesized using a general host–guest strategy, *Nat. Chem.* 12 (2020) 764–772, <https://doi.org/10.1038/s41557-020-0473-9>.
- [32] A. Zitolo, V. Goellner, V. Arnel, M.T. Sougrati, T. Mineva, L. Stievano, E. Fonda, F. Jaouen, Identification of catalytic sites for oxygen reduction in iron- and nitrogen-doped graphene materials, *Nat. Mater.* 14 (2015) 937–942, <https://doi.org/10.1038/nmat4367>.
- [33] R. Li, P. Rao, D. Wu, J. Li, P. Deng, Z. Miao, X. Tian, Understanding the bifunctional trends of Fe-based binary single-atom catalysts, *Adv. Sci.* 2301566 (2023) 1–10, <https://doi.org/10.1002/adv.202301566>.
- [34] H. Li, S. Di, P. Niu, S. Wang, J. Wang, L. Li, A durable half-metallic diatomic catalyst for efficient oxygen reduction, *Energy Environ. Sci.* 15 (2022) 1601–1610, <https://doi.org/10.1039/d1ee03194e>.
- [35] J. Liu, M. Jiao, L. Lu, H.M. Barkholtz, Y. Li, L. Jiang, Z. Wu, D.J. Liu, L. Zhuang, C. Ma, J. Zeng, B. Zhang, D. Su, P. Song, W. Xing, W. Xu, Y. Wang, Z. Jiang, G. Sun, High performance platinum single atom electrocatalyst for oxygen reduction reaction, *Nat. Commun.* 8 (1) (2017) 9, <https://doi.org/10.1038/ncomms15938>.
- [36] S. Sun, Y. Sun, Y. Zhou, J. Shen, D. Mandler, R. Neumann, Z.J. Xu, Switch of the rate-determining step of water oxidation by spin-selected electron transfer in spinel oxides, *Chem. Mater.* 31 (2019) 8106–8111, <https://doi.org/10.1021/acs.chemmater.9b02737>.
- [37] J. Cheng, C. Lyu, H. Li, J. Wu, Y. Hu, B. Han, K. Wu, M. Hojamberdiev, D. Geng, Steering the oxygen reduction reaction pathways of N-carbon hollow spheres by heteroatom doping, *Appl. Catal. B Environ.* 327 (2023), 122470, <https://doi.org/10.1016/j.apcatb.2023.122470>.
- [38] J. Li, Y. Kang, Z. Lei, P. Liu, Well-controlled 3D flower-like CoP<sub>3</sub>/CeO<sub>2</sub>/C heterostructures as bifunctional oxygen electrocatalysts for rechargeable Zn-air batteries, *Appl. Catal. B Environ.* 321 (2023), 122029, <https://doi.org/10.1016/j.apcatb.2022.122029>.
- [39] W. Cheng, P. Yuan, Z. Lv, Y. Guo, Y. Qiao, X. Xue, X. Liu, W. Bai, K. Wang, Q. Xu, J. Zhang, Boosting defective carbon by anchoring well-defined atomically dispersed metal-N<sub>4</sub> sites for ORR, OER, and Zn-air batteries, *Appl. Catal. B Environ.* 260 (2020), 118198, <https://doi.org/10.1016/j.apcatb.2019.118198>.
- [40] Y. Ma, J. Li, X. Liao, W. Luo, W. Huang, J. Meng, Q. Chen, S. Xi, R. Yu, Y. Zhao, L. Zhou, L. Mai, Heterostructure design in bimetallic phthalocyanine boosts oxygen reduction reaction activity and durability, *Adv. Funct. Mater.* 30 (2020), 2005000, <https://doi.org/10.1002/adfm.202005000>.
- [41] K.M. Zhao, S. Liu, Y.Y. Li, X. Wei, G. Ye, W. Zhu, Y. Su, J. Wang, H. Liu, Z. He, Z. Y. Zhou, S.G. Sun, Insight into the mechanism of axial ligands regulating the catalytic activity of Fe-N<sub>4</sub> sites for oxygen reduction reaction, *Adv. Energy Mater.* 12 (2022) 1–7, <https://doi.org/10.1002/aenm.202103588>.
- [42] Y. Sun, X. Ren, S. Sun, Z. Liu, S. Xi, Z.J. Xu, engineering high-spin state cobalt cations in spinel zinc cobalt oxide for spin channel propagation and active site enhancement in water oxidation, *Angew. Chem. Int. Ed.* (2021) 14536–14544, <https://doi.org/10.1002/anie.202102452>.
- [43] N. Ramaswamy, U. Tylus, Q. Jia, S. Mukerjee, Activity descriptor identification for oxygen reduction on nonprecious electrocatalysts: linking surface science to coordination chemistry, *J. Am. Chem. Soc.* 135 (2013) 135, <https://doi.org/10.1021/ja405149m>.
- [44] M.-S. Liao, S. Scheiner, Electronic structure and bonding in metal porphyrins, metal=Fe, Co, Ni, Cu, Zn, *J. Chem. Phys.* 117 (2002) 205–219, <https://doi.org/10.1063/1.1480872>.
- [45] Z. yuan Mei, G. Zhao, C. Xia, S. Cai, Q. Jing, X. Sheng, H. Wang, X. Zou, L. Wang, H. Guo, B.Y. Xia, Regulated high-spin state and constrained charge behavior of active cobalt sites in covalent organic frameworks for promoting electrocatalytic oxygen reduction, *Angew. Chem. Int. Ed.* 62 (2023), <https://doi.org/10.1002/anie.202303871>.
- [46] L. Wang, Z. Mei, Q. An, X. Sheng, Q. Jing, W. Huang, X. Wang, X. Zou, H. Guo, Modulating the electronic spin state of atomically dispersed iron sites by adjacent zinc atoms for enhanced spin-dependent oxygen electrocatalysis, *Chem. Catal.* (2023), <https://doi.org/10.1016/j.checat.2023.100758>.
- [47] R. Zhou, Y. Zheng, M. Jaroniec, S. Qiao, Determination of the electron transfer number for the oxygen reduction reaction: from theory to experiment, *ACS Catal.* 6 (2016) 4728, <https://doi.org/10.1021/acscatal.6b01581>.
- [48] Z. Lu, B. Wang, Y. Hu, W. Liu, Y. Zhao, R. Yang, Z. Li, J. Luo, B. Chi, Z. Jiang, M. Li, S. Mu, S. Liao, J. Zhang, X. Sun, An isolated zinc–cobalt atomic pair for highly active and durable oxygen reduction, *Angew. Chem. Int. Ed.* 58 (2019) 2622–2626, <https://doi.org/10.1002/anie.201810175>.
- [49] Y. Mun, S. Lee, K. Kim, S. Kim, S. Lee, J.W. Han, J. Lee, Versatile strategy for tuning ORR activity of a single Fe-N<sub>4</sub> site by controlling electron-withdrawing/donating properties of a carbon plane, *J. Am. Chem. Soc.* 141 (2019) 6254–6262, <https://doi.org/10.1021/jacs.8b13543>.